

Interplay of many-body interactions and quasiperiodic disorder in the all-bands-flat diamond chainAamna Ahmed¹, Nilanjan Roy², and Auditya Sharma¹¹*Department of Physics, Indian Institute of Science Education and Research, Bhopal, Madhya Pradesh 462066, India*²*Centre for Condensed Matter Theory, Department of Physics, Indian Institute of Science, Bangalore 560012, India*

(Received 3 April 2023; accepted 19 May 2023; published 7 June 2023)

We study the effects of quasiperiodic Aubry-André (AA) disorder and interactions on a one-dimensional all-bands-flat (ABF) diamond chain. We consider the application of disorder in two ways: A symmetric one, where the same disorder is applied to the top and bottom sites of a unit cell, and an antisymmetric one, where the disorder applied to the top and bottom sites are of equal magnitude but with opposite signs. The single-particle wave-packet dynamics for the clean system and when the disorder is applied symmetrically show quantum caging; in the antisymmetric case, the wave packet spreads over the entire lattice. These results agree with our previous study, where compact localization was observed in the case of the clean system and for symmetrically disordered diamond lattices. In the presence of nearest-neighbor interactions, nonergodic phases are observed in the case of a clean system and symmetrical disorder; at higher disorder strengths, we find an MBL-like phase in the symmetric case. However, many-body nonequilibrium dynamics of the system from carefully engineered initial states exhibit quantum caging. In the antisymmetric case, a nonergodic mixed phase, a thermal phase, and an MBL-like phases, respectively, are observed at low, intermediate, and high disorder strengths. We observe an absence of caging and initial state dependence (except at the intermediate disorder strength) in the study of nonequilibrium dynamics.

DOI: [10.1103/PhysRevB.107.245110](https://doi.org/10.1103/PhysRevB.107.245110)**I. INTRODUCTION**

Flat-band (FB) systems, which are characterized by highly degenerate energy levels and support *compact localized eigenstates* (CLS) [1,2], has been a subject of great interest over the last decade [3–7], although the concepts are older where the term Aharanov Bohm (AB) caging [8–11] has been used. Compact localized states span strictly over a few unit cells, with zero probability amplitude elsewhere in contrast to Anderson localization [12], where the “spread” of a state dies down exponentially. While Anderson localization observed in noninteracting disordered systems is now a mature topic with a large body of literature around it, the localization characteristics of quantum systems in the presence of both disorder and interactions [13–18] is an actively evolving area of research. A prominent example is the phenomenon of *many-body localization* (MBL) [19–25] where the system fails to thermalize even in the presence of interactions. Translationally invariant single-particle flat-band networks coupled with many-body interactions have also recently gained a lot of attention [26–31]. These models exhibit nonergodic behavior with a lack of transport of particles for any interaction strength exhibiting *many-body flat-band localization* (MBFBL) [27,31]. This naturally motivates the study of flat-band systems subjected to both disorder and interactions [32–34].

In one of our previous paper [32], we systematically investigated the effects of turning on interactions in the presence of uniform disorder on the all-bands-flat (ABF) diamond chain. This model shows a nonergodic mixed phase at low disorder strength, separated from the MBL phase at high disorder strength by a thermal phase at intermediate disorder strength. The addition of disorder to flat-band systems is known to yield exotic behavior [35–37]. In our recent paper [37], we investi-

gated the effect of a quasiperiodic Aubry-André (AA) on-site disorder [38,39] on the ABF diamond chain. We found that the symmetry of the applied external potential plays a crucial role. With a symmetric disorder, it is possible to completely destroy the degeneracy and still preserve the compact localization of the eigenstates [40]. However, when the disorder is applied in an antisymmetric fashion, both the degeneracy and compact localization are destroyed and a robust *flat-band-based multifractality* (FBM) [41–43] is observed in an extensive region of the phase diagram. In the present paper, we study the effects of interactions on the ABF diamond chain both in the absence and presence of quasiperiodic disorder.

We begin by exploring single-particle dynamics, which shows quantum caging in the long-time limit for both the zero-disorder and symmetric disorder cases. However, when the disorder is applied in an antisymmetric manner since the compact localization of the eigenstates is destroyed [37], the time-evolved state also displays a spreading over all the lattice sites. We next investigate the properties of the clean system when interactions are turned on. The system manifests nonergodic phases at all interaction strengths in the zero-disorder case. However, from a study of nonequilibrium dynamics, we conclude that for some specially engineered initial states, many-body systems exhibit caging behavior independent of the strength of the interaction.

In the simultaneous presence of disorder and interactions, the symmetry of the applied disorder is again crucial. A symmetric disorder coupled with interactions yields nonergodic phases in the low and intermediate disorder regimes and MBL-like behavior in the high disorder regime. We find that the dynamics is dependent on the initial state; in particular, we observe quantum caging for specific engineered initial states.

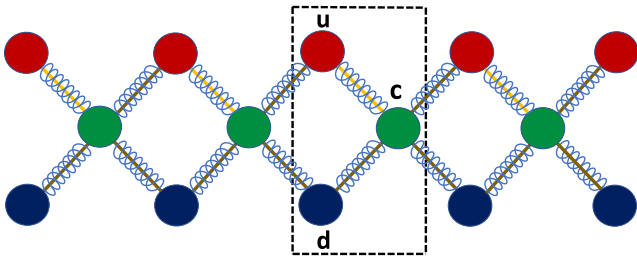


FIG. 1. Schematic representation of the diamond lattice with the u (up), d (down), and c (centre) sites of a representative unit cell confined by the black dashed lines. Nearest-neighbor interaction V is represented by wiggly blue lines.

The antisymmetric application of disorder leads to a mixed nonergodic phase at low disorder strength, a thermal phase at intermediate disorder strength, and an MBL-like phase at high disorder strength. The mixed phase obtained at low disorder strength is attributed to the presence of multifractal states in the single particle limit. Although we find initial state dependence in the nonequilibrium dynamics (except for intermediate disorder strengths, which yield a thermal phase), no quantum caging behavior is seen.

This paper is organized as follows. In Sec. II, we discuss the details of the model. In Sec. III, we discuss the effects of AA disorder on the single-particle dynamics in the disorder-free, symmetric, and antisymmetric cases. Section IV discusses the effects of interactions on the clean ABF diamond chain. Section V explores the symmetric application of quasiperiodic AA disorder on the interacting system. Section VI discusses the interplay of antisymmetric application of disorder and interactions. We then summarize our results in Sec. VII.

II. MODEL

We study the ABF diamond lattice, where the k th unit cell consists of three sites $\alpha_k = \{u_k, d_k, c_k\}$ (see Fig. 1). The fermionic creation operators acting at the u (up), c (center), and d (down) sites respectively in the k th unit cell are \hat{u}_k^\dagger , \hat{c}_k^\dagger , and \hat{d}_k^\dagger and the Hamiltonian is

$$\hat{H} = \hat{H}_{\text{hop}} + \hat{H}_{\text{os}} + \hat{H}_{\text{int}}, \quad (1)$$

where

$$\begin{aligned} \hat{H}_{\text{hop}} &= -J \sum_{k=1}^{N/3} (-\hat{u}_k^\dagger \hat{c}_k + \hat{d}_k^\dagger \hat{c}_k + \hat{c}_k^\dagger \hat{u}_{k+1} + \hat{c}_k^\dagger \hat{d}_{k+1} + \text{H.c.}), \\ \hat{H}_{\text{os}} &= \sum_{k=1}^{N/3} (\zeta_k^u \hat{u}_k^\dagger \hat{u}_k + \zeta_k^c \hat{c}_k^\dagger \hat{c}_k + \zeta_k^d \hat{d}_k^\dagger \hat{d}_k), \\ \hat{H}_{\text{int}} &= V \sum_{k=1}^{N/3} (\hat{u}_k^\dagger \hat{u}_k \hat{c}_k^\dagger \hat{c}_k + \hat{d}_k^\dagger \hat{d}_k \hat{c}_k^\dagger \hat{c}_k + \hat{c}_k^\dagger \hat{c}_k \hat{u}_{k+1}^\dagger \hat{u}_{k+1} \\ &\quad + \hat{c}_k^\dagger \hat{c}_k \hat{d}_{k+1}^\dagger \hat{d}_{k+1}). \end{aligned} \quad (2)$$

The total number of lattice sites is denoted by N , which should be a multiple of 3 owing to the unit-cell structure of the periodic lattice. The hopping amplitude is J , which

is taken to be 1 for simplicity, and V is the strength of the nearest-neighbor interaction. For each site of the k th unit cell, we include independent on-site Aubry-André potentials

$$\zeta_k^\alpha = \lambda_\alpha \cos(2\pi kb + \theta_p), \quad (3)$$

where the strength of the potential is λ_α and the quasiperiodicity parameter b is taken to be the golden mean $(\sqrt{5} - 1)/2$. The arbitrary global phase θ_p is chosen randomly from a uniform random distribution $[0, 2\pi]$. Here we consider two types of correlations between the on-site energies on the up “ u ” and down “ d ” sites: A symmetric configuration in which $\zeta_k^u = \zeta_k^d$ and an antisymmetric configuration in which $\zeta_k^u = -\zeta_k^d$.

In the clean noninteracting limit, the ABF diamond chain possesses three flat bands at energies $\pm 2, 0$ and no dispersive band. Consequently, the system is a good insulator, possessing only compact localized eigenstates. The system is highly degenerate, with the CLS occupying two unit cells. The other states corresponding to each flat band can be obtained by translating by an integer multiple of unit cells along the lattice. In the presence of symmetric disorder, remarkably, the eigenstates continue to be compactly localized in the original basis [37] although the translation symmetry and, thus, the flat-band structure are broken. On the other hand, when the potential is applied in an antisymmetric manner, we find neither degeneracy nor compact localization [37], but a novel kind of *flat-band-based multifractality*.

III. SINGLE-PARTICLE DYNAMICS

In this section, we explore the single-particle properties with the help of nonequilibrium dynamics of the particle density and the return probability. We will see that these results are consistent with the static properties of the eigenstates we obtained in our earlier study [37]. We study the dynamics by considering two initial states, one where the single-particle occupies the lattice site “ c ” of the k^{th} unit cell ($|\psi_{\text{in}}\rangle = |c_k\rangle$) and the other where it occupies the lattice site “ d ” of the k th unit cell ($|\psi_{\text{in}}\rangle = |d_k\rangle$). We choose $k = N/6$ so as to focus on the sites of the central unit cell—the total number of unit cells is $N/3$. Once the initial state is fixed, we obtain the time evolved state at time t using the relation $|\psi(t)\rangle = \sum_{m=1}^N \psi_m(t) |m\rangle = e^{-iHt} |\psi_{\text{in}}\rangle$ where m denotes the site index that runs over all the N sites, i.e., $1, 2, \dots, m, \dots, N$. Also, selecting the “ u ” site yields similar results as the “ d ” site case; thus, we do not show the results here.

A. Zero-disorder case

We first study the system in the clean limit. We begin by investigating the evolution of the particle density where $p_m(t) = |\psi_m(t)|^2$ is the probability of site m being occupied at time t . When the initial state is chosen to be $|\psi_{\text{in}}\rangle = |c_k\rangle$, the particle remains compactly localized in two unit cells at all instances of time [see Fig. 2(a)]. On the other hand, with the initial state taken to be $|\psi_{\text{in}}\rangle = |d_k\rangle$, we observe that the particle becomes compactly localized in three unit cells at all instances of time [see Fig. 2(c)]. Also, the number of unit cells in which the particle is compactly localized is robust with increasing system size.

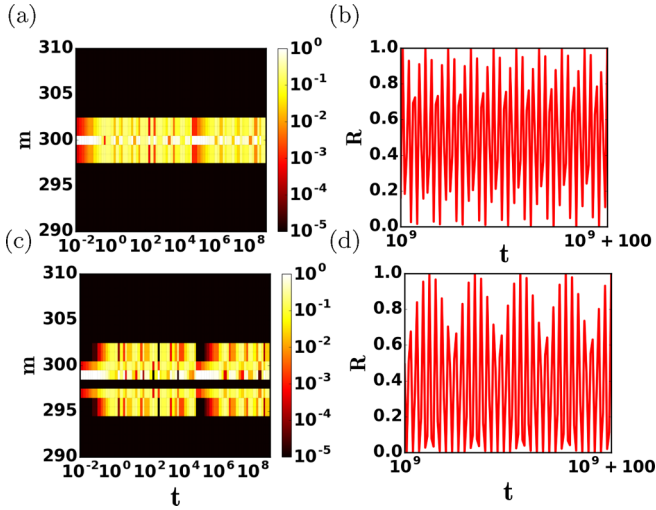


FIG. 2. Clean system: The particle density (whose value is represented by a color according to the code shown) as a function of time t , with m denoting the site index, for a single-particle initially at the (a) c site and (c) d site of the 100th unit cell for system size $N = 600$ (200 unit cells) in the ABF diamond lattice. The return probability $R(t)$ as a function of time t for a particle initially at the (b) c site and (d) d site of the 100th unit cell.

We next calculate the return probability, which is defined as

$$R(t) = |\langle \psi_{\text{in}} | \psi(t) \rangle|^2. \quad (4)$$

It is the probability of finding the particle in the initial state after a time t . In the disorder-free limit, we have plotted the return probability starting from both the initial states in the

long-time limit $t = 10^9$ in Figs. 2(b) and 2(d). The spectrum is highly degenerate in the disorder-free limit, yielding three energy levels, i.e., $E = \pm 2, 0$. Since the return probability is related to the level spacing of the energy levels, $R(t)$ shows oscillatory behavior [44,45]. We conclude that the dynamics of the clean system is dependent on the initial state.

B. Symmetric-disorder case

We next consider the introduction of disorder in the symmetric configuration,

$$\zeta_k^u = \zeta_k^d \quad \text{and} \quad \zeta_k^c = 0. \quad (5)$$

We have previously observed [37] that in the single-particle limit, although the degeneracy of all the flat bands is lifted, the eigenstates are found to be compactly localized in two unit cells at all strengths of disorder. In the disorder-free limit, a series of transformations [37] converts the diamond lattice into a set of entirely uncoupled sites. In the case of symmetric disorder, this transformation results in a lattice made of three-site unit cells but with an absence of intercell hopping, indicating the preservation of the CLSs.

For the initial state $|\psi_{\text{in}}\rangle = |c_k\rangle$, from the evolution of the particle density, it can be observed that the state is compactly localized over two unit cells in the low, intermediate, and high disorder regimes [see Figs. 3(a)–3(c)]. However, at higher disorder $\lambda = 100$, the site on which the particle is initially localized shows a large occupation probability at all times, as indicated by the central white patch in Fig. 3(c). Also, in the long-time limit, the return probability has finite magnitude ≈ 0.5 for $\lambda = 0.01, 2$ and a magnitude close to unity for $\lambda = 100$, as shown in Fig. 3(d). We then study the dynamics for

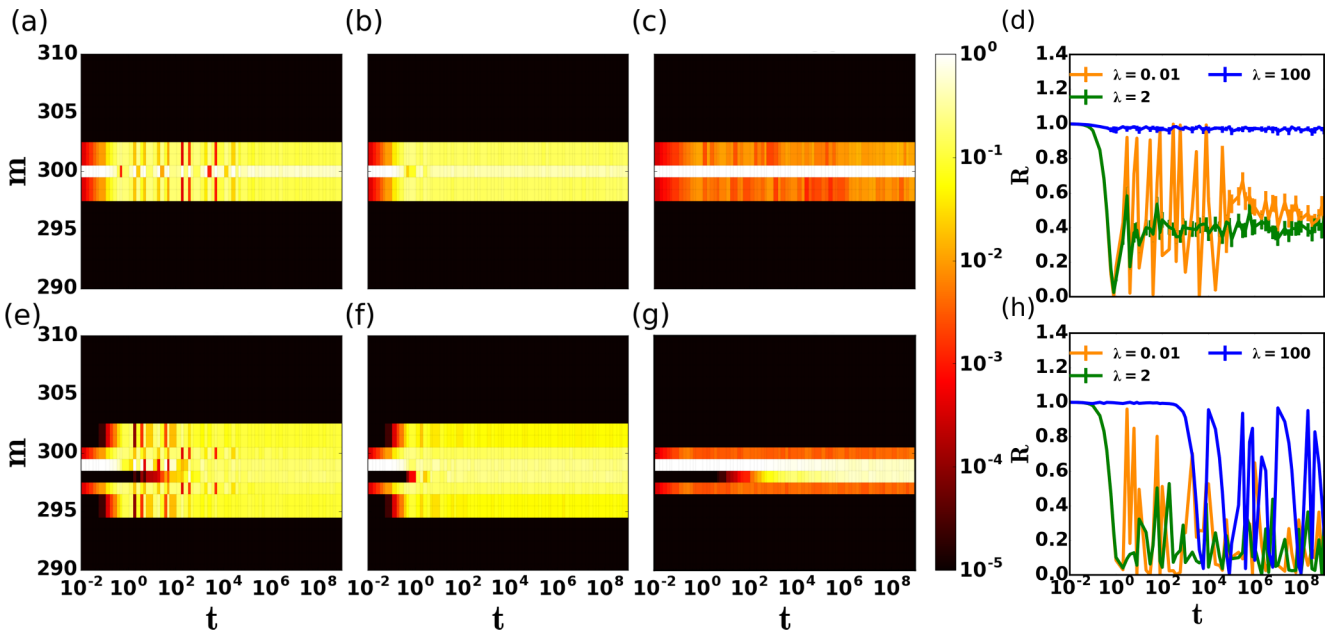


FIG. 3. In the symmetric case, the particle density (whose value is represented by a color according to the code shown) as a function of time t , with m denoting the site index, for a single particle initially at the c site of the 100th unit cell with increasing disorder strength (a) $\lambda = 0.01$, (b) $\lambda = 2$, and (c) $\lambda = 100$; and (d) evolution of the return probability R . For a single particle initially at the d site of the 100th unit cell, the particle density as a function of time t for (e) $\lambda = 0.01$, (f) $\lambda = 2$, (g) $\lambda = 100$, and (h) evolution of the return probability R . Here system size is $N = 600$, and the number of disorder realizations is 100.

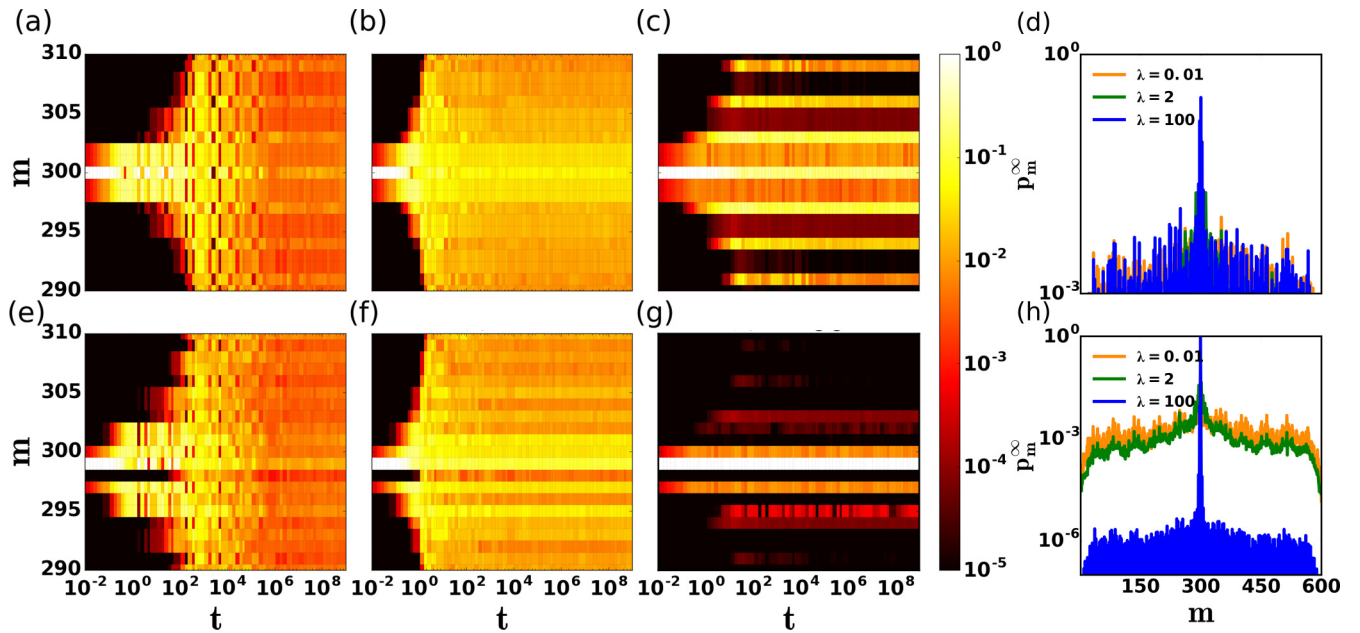


FIG. 4. In the antisymmetric case, the particle density (whose value is represented by a color according to the code shown) as a function of time t , with m denoting the site index, for a single particle initially at the c site of the 100th unit cell with increasing disorder strength (a) $\lambda = 0.01$, (b) $\lambda = 2$, and (c) $\lambda = 100$; and (d) particle density at $t = 10^9$ for various strengths of disorder. For a single particle initially at the d site of the 100th unit cell, the particle density as a function of time t for (e) $\lambda = 0.01$, (f) $\lambda = 2$, and (g) $\lambda = 100$; and (h) particle density at $t = 10^9$ for various strengths of disorder. Here system size is $N = 600$, and averaging over 100 disorder realizations have been considered.

the initial state $|\psi_{\text{in}}\rangle = |d_k\rangle$. From the evolution of the particle density, we observe that at all strengths of disorder, the state is compactly localized over three unit cells [see Figs. 3(e)–3(g)]. The return probability in the long-time limit has a finite value at all disorder strengths, as shown in Fig. 3(h).

On the introduction of a symmetric disorder, the spectrum becomes dispersive, although the eigenstates are compactly localized. We obtain nondegenerate energy levels, whose magnitude depends on the disorder strength. As the return probability involves the contribution of various energy levels through the time evolution operator $U(t) = e^{-iHt}$, its periodicity is affected by the various energy levels and the initial state.

There is a second way in which the symmetric disorder can be introduced wherein only the c sites are perturbed,

$$\zeta_k^u = \zeta_k^d = 0 \quad \text{and} \quad \zeta_k^c \neq 0. \quad (6)$$

In this case, we know [37] that while the degeneracy is broken for the upper and lower bands, the flat band at $E = 0$ remains robust even at higher disorder strengths. We have checked that the single-particle dynamics within this scenario yields qualitatively similar results as discussed above.

C. Antisymmetric-disorder case

We next consider the application of the AA potential in an antisymmetric manner, defined by

$$\zeta_k^u = -\zeta_k^d = \lambda \cos(2\pi kb + \theta_p) \quad \text{and} \quad \zeta_k^c = 0. \quad (7)$$

In the single-particle limit, we observed [37] that the tiniest of perturbation lifted the degeneracy, and the eigenstates were no longer compactly localized. Further, we also reported the existence of a central band with extended nonergodic

(multifractal) eigenstates separated from the Anderson localized states by a fractal mobility edge $|E| < 4/\lambda$ [46].

From the evolution of the particle density, we observe that for the initial state $|\psi_{\text{in}}\rangle = |c_k\rangle$ the wavefunction spreads over the entire lattice with time t at all strengths of the disorder [see Figs. 4(a)–4(c)]. The same can be observed in the long-time limit $t = 10^9$ [see Fig. 4(d)], with occupation probability p_m^∞ , spreading nonuniformly over the entire space at all strengths of disorder, which is a signature of the multifractal states, as observed in the phase diagram in the static case [37]. The results are qualitatively the same for the dynamics associated with the other initial state $|\psi_{\text{in}}\rangle = |d_k\rangle$ as shown in Figs. 4(e)–4(h). In both cases, in the higher disorder regime $\lambda = 100$, we observe that the site on which the particle is initially localized shows a large occupation probability in the long-time limit [see Figs. 4(d) and 4(h)]. For low and intermediate disorder, we have also checked (results not shown here) that the return probability $R(t)$ in the long-time limit is of the order of $O(10^{-2})$ due to the contribution of a large fraction of multifractal eigenstates. At higher disorder strengths, it is ≈ 0.4 for $|\psi_{\text{in}}\rangle = |c_k\rangle$ and ≈ 1 for $|\psi_{\text{in}}\rangle = |d_k\rangle$ owing to the presence of a large fraction of localized eigenstates.

IV. INTERACTING DISORDER-FREE SYSTEM

In this section, we study the effects of the interaction V on the ABF diamond lattice in the zero-disorder limit. We investigate the properties of the eigenstates with the help of the many-particle inverse participation ratio (MIPR) and the one-particle density matrix (OPDM). We also explore the dynamics of the particle density, entanglement entropy and return probability. For a system size N with N_p being the particle number, the dimension of the Hilbert space is $D = \binom{N}{N_p}$

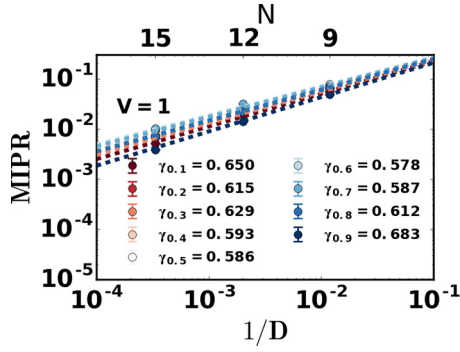


FIG. 5. MIPR averaged over the eigenstates in the energy window $[\varepsilon - 0.01, \varepsilon + 0.01]$ with $1/D$ (D is the dimension of the Hilbert space) where $\varepsilon = 0.1, 0.2, \dots, 0.9$, for a fixed interaction strength $V = 1$. Here system sizes considered are $N = 9, 12$, and 15 , and the filling fraction is fixed as $\nu = 1/3$.

and the filling fraction is represented by $\nu = \frac{N_p}{N}$. Using exact diagonalization, we obtain the many-body energy spectra E_i and the normalized eigenstates $|\psi\rangle_i$, where $i = 1, 2, \dots, D$.

Expanding a normalized eigenstate $|\Psi\rangle$ in the particle number constrained space as $|\Psi\rangle = \sum_{i=1}^D C_i |i\rangle$, we compute the many-particle inverse participation ratio (MIPR),

$$\text{MIPR} = \sum_{i=1}^D |C_i|^4. \quad (8)$$

For a perfect delocalized eigenstate $\text{MIPR} = O(1)/D$, while for an extremely localized eigenstate, $\text{MIPR} = O(1)$. Here we study the scaling of MIPR with D , using the relation $\text{MIPR} \propto \frac{1}{D^\gamma}$. γ is close to 0 in the MBL phase, while in a perfectly delocalized many-body phase $\gamma = 1$ and in the nonergodic many-body phase $0 < \gamma < 1$ [47].

In Fig. 5, we fix the filling fraction $\nu = 1/3$ and extract γ by increasing the system size N . Using the relation $\varepsilon_i = \frac{E_i - E_1}{E_D - E_1}$, where E_1 and E_D are the ground state and maximum energy levels, respectively, the energy levels are rescaled to lie within the range $0 \leq \varepsilon_i \leq 1$. We then study MIPR averaged over the states in the energy windows, which are specified as $[\varepsilon - 0.01, \varepsilon + 0.01]$, where $\varepsilon = 0.1, 0.2, \dots, 0.9$ at $V = 1$. From the energy-resolved study, we observe that $0.57 \leq \gamma_\varepsilon \leq 0.68$ over the entire energy spectrum, indicating the existence of a nonergodic phase.

The localization characteristics of a many-body system can also be explored with the help of the one-particle density matrix (OPDM) [48–50]. The OPDM ρ_o for any many-body eigenstate $|\Psi\rangle$ is defined as

$$(\rho_o)_{ij} = \langle \Psi | a_i^\dagger a_j | \Psi \rangle, \quad (9)$$

where we have renamed the fermion operators at the various sites of the different unit cells as $(u_1, d_1, c_1, u_2, d_2, c_2, \dots, u_k, d_k, c_k) = (a_1, a_2, a_3, \dots, a_N)$ where a_i^\dagger (a_i) creates(annihilates) a fermion on-site i which runs from $i = 1, 2, \dots, N$. A compact way to define these new operators is to simply write

$$\begin{aligned} u_k &= a_{3(k-1)+1}, \\ d_k &= a_{3(k-1)+2}, \\ c_k &= a_{3(k-1)+3}, \end{aligned} \quad (10)$$

where $k = 1, 2, \dots, \frac{N}{3}$ runs over the unit cells. The diagonalization of the OPDM results in a basis of single-particle eigenstates called the natural orbitals $|\phi_\alpha\rangle$, with $\alpha = 1, 2, \dots, N$ and their occupations (eigenvalues) denoted by n_α ,

$$\rho_o |\phi_\alpha\rangle = n_\alpha |\phi_\alpha\rangle. \quad (11)$$

The trace of the OPDM is equal to the total number of particles in the system $\text{tr}(\rho_o) = \sum_{\alpha=1}^N n_\alpha = N_p$, and the natural orbitals are ordered with decreasing occupation: $n_1 \geq n_2 \geq \dots \geq n_N$.

These natural orbitals are localized in the MBL phase and delocalized in the ergodic phase. This behavior of the natural orbitals is a many body effect since, without interactions, the natural orbitals of the single-particle energy eigenstates are all localized. In a noninteracting system, each many-body eigenstate $|\Psi\rangle$ is a Slater determinant of N_p single-particle states, with the occupation spectrum $n_\alpha = 1$ for all $\alpha \leq N_p$ and zero otherwise at any strength of disorder. In the MBL phase, all the natural orbitals corresponding to $\alpha \leq N_p$ remain almost fully occupied ($\langle n_\alpha \rangle \approx 1$), while the others remain almost unoccupied ($\langle n_\alpha \rangle \approx 0$), resulting in a discontinuity $\delta n = n_{N_p+1} - n_{N_p}$ that is close to unity. In the thermal phase, the occupations of all the orbitals approach the mean filling fraction $\langle n_\alpha \rangle \approx \nu$. In the ergodic phase, the occupation spectrum is consistent with the eigenstate thermalization hypothesis, while in the MBL phase, the occupations preserve a discontinuity at an emergent Fermi edge.

From the occupation spectrum, the one-particle occupation entropy can be calculated as follows:

$$S_o = -\text{tr} \rho_o \ln \rho_o = -\sum_{\alpha} n_\alpha \ln(n_\alpha). \quad (12)$$

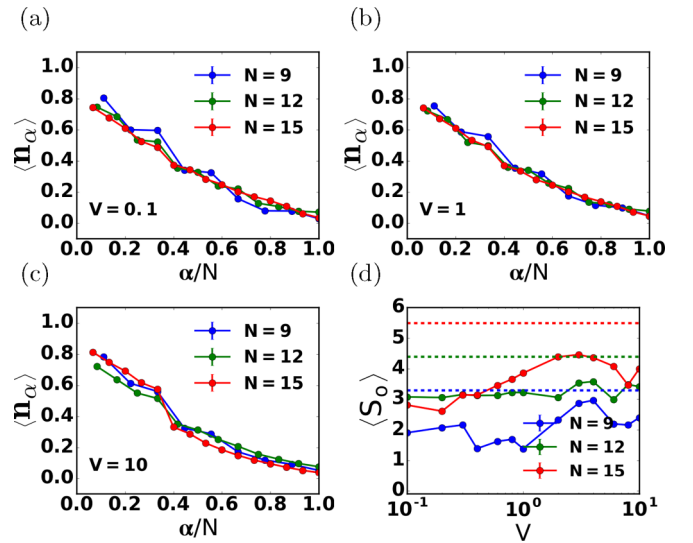


FIG. 6. Occupation spectrum $\langle n_\alpha \rangle$ with scaled index α/N at fixed interaction strengths (a) $V = 0.1$, (b) $V = 1$, and (c) $V = 10$, for different system sizes $N = 9, 12, 15$ and filling fraction $\nu = 1/3$. (d) The average OPDM entropy S_o with increasing interaction strength V . Dashed lines denote the maximal value of S_o . Averaging has been performed over the eigenstates in the energy window $\varepsilon = [0.54, 0.57]$.

The one-particle occupation entropy is large and proportional to the system size in the delocalized phase, corresponding to the volume law of thermal states. In contrast, in the localized phase, it is close to 0. In the ergodic phase $\langle n_\alpha \rangle \approx \nu$, hence for a filling fraction $\nu = 1/3$ considered here, the maximal value of S_o will be $(N/3)\ln 3$. Thus in the thermal phase, it corresponds to the volume law displayed by many-body eigenstates, while it approaches 0 in the localized phase.

In Figs. 6(a)–6(c), we have plotted the occupation spectrum $\langle n_\alpha \rangle$ at different interaction strengths $V = 0.1, 1$, and 10 and over a specific energy window $\varepsilon = [0.54, 0.57]$. We observe that the occupations are not close to 1 or 0, indicating the absence of MBL. Further deep in the thermal phase, $\langle n_\alpha \rangle$ are expected to become system size independent at the filling fraction ($\nu = 1/3$ here), while splaying out on either side in a characteristic system-size-dependent manner; here, we only see a monotonic decrease with almost no system size dependence throughout. We conclude that the presence of interaction in the ABF diamond lattice results in a nonergodic phase—this is in agreement with the results of MIPR. We also study the OPDM entropy S_o [see Fig. 6(d)] for the states corresponding to the energies $\varepsilon = [0.54, 0.57]$. We observe that S_o does not reach its maximal value [dashed lines in Fig. 6(d)], nor does it decrease to 0 at any interaction strength V , and indicates nonergodic behavior.

In Sec. III from our discussion of the single-particle dynamics, we have seen how the number of unit cells occupied by the time-evolving state depends on the initial state. Here we study many-body nonequilibrium dynamics with the help of particle density, entanglement entropy and return probability. The study of entanglement entropy [51,52] serves as a quantifier of localization in many-body systems. For the many-body state $|\psi\rangle$, one can calculate the density matrix $\rho = |\psi\rangle\langle\psi|$. The system is then divided into two parts, one with N_A number of sites and the other with $N_B = N - N_A$ sites. The reduced density matrix (RDM) is calculated by tracing over the subsystem B as $\rho_A = \text{Tr}_B(\rho)$, and the entanglement entropy is given by $S_A = -\text{Tr}(\rho_A \ln \rho_A)$.

In order to understand the interplay of initial configuration and interaction V , we consider two types of initial states for the system size $N = 18$ and a filling fraction $\nu = 1/6$. In the first case, we consider an initial state of the density wave type with particles on c sites of alternate unit cells [32],

$$|\psi_{\text{in}}^c\rangle = \prod_{i=1}^{N/6} \hat{c}_{2i-1}^\dagger |0\rangle. \quad (13)$$

In the second type of initial state, the d sites of alternate unit cells are occupied,

$$|\psi_{\text{in}}^d\rangle = \prod_{i=1}^{N/6} \hat{d}_{2i-1}^\dagger |0\rangle. \quad (14)$$

Figures 7(a)–7(c) show the dynamics starting from the initial state given by Eq. (13). When the particles are arranged in a manner such that $|h - l| \geq 2$ where h, l are the unit cell indices of any pair of particles, we observe distinct CLSs for each particle as shown by the evolution of the particle density in Fig. 7(a). The particles show caging behavior and remain unaffected by the interactions here. The same can be

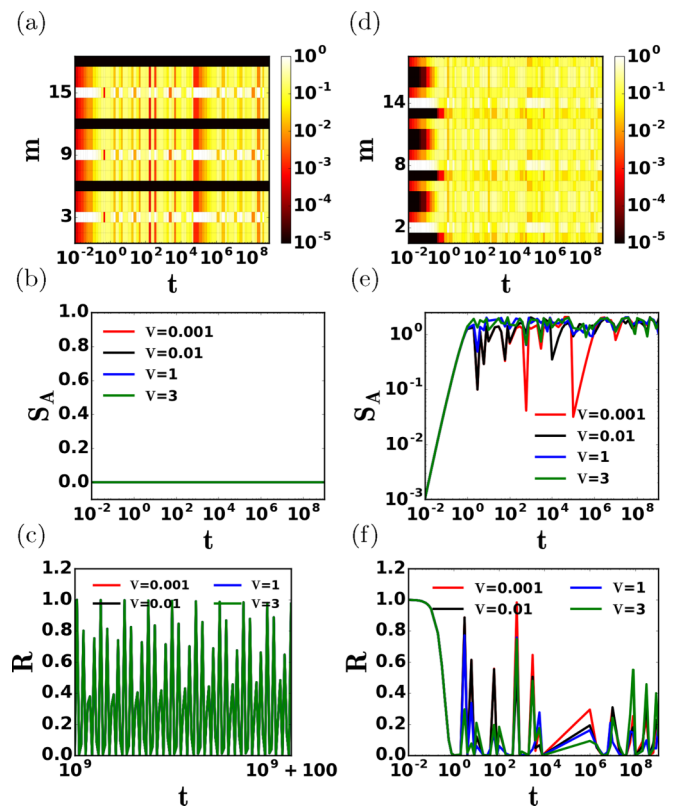


FIG. 7. For the initial state given by Eq. (13), (a) the particle density (whose value is represented by a color according to the code shown) as a function of time t , where m is the site index at interaction strength $V = 1$, (b) the entanglement entropy S_A as a function of time t for a subsystem of size $N_A = N/3$, and (c) the return probability R as a function of time t for interaction strengths $V = 0.001, 0.01, 1$ and 3. [(d)–(f)] Corresponding plots for the initial state given by Eq. (14). For all cases, $N = 18$ and $\nu = 1/6$.

observed from the evolution of the entanglement entropy S_A , where $N_A = 1/3$ in Fig. 7(b). We observe that at all interaction strengths, there is zero entanglement between the two subsystems, indicating that the compact localized states are unaffected by interaction strength V . Also, we observe that the return probability shows perfect oscillations [see Fig. 7(c), where time axis is shown on a linear scale to highlight the oscillations] in the long-time limit independent of the strength of interaction.

We then consider the initial configuration given by Eq. (14), corresponding to a $1/6$ filling fraction. However, the CLS corresponding to the single particles spans over three unit cells, as shown in Fig. 2(c). Consequently, from the evolution of the particle density, we observe an overlap between the CLS belonging to different particles in Fig. 7(d). This suggests that interaction among the initially caged particles comes into play. The same can also be observed from the evolution of S_A , where we plot the entanglement by considering the subsystem size $N_A = 1/3$. After an initial transient till $t \approx 1$, independent of the interaction strength V , the entanglement saturates to a significant value indicating a nonergodic phase. From Fig. 7(f), we observe that the return probability displays continual oscillations about a nonzero mean value, although it does not reach 1. A closer look at this figure in a linear

scale shows that the oscillations are interaction dependent, mainly controlled by the interaction-dependent gaps between the degenerate bands of the many-body energy spectrum. These energy gaps are constant throughout the dynamics, and hence, the associated terms present in the return probability do not vanish due to phase randomization, giving rise to energy gap-dependent fluctuations in return probability throughout the dynamics. This scenario is typical of a clean degenerate system perturbed with many-body interactions [32]. This behavior is also consistent with the nonergodic phase argued from the previous quantities.

V. INTERACTIONS AND SYMMETRIC DISORDER

In this section, we study the interplay of symmetric disorder and interactions. Specifically, we study the effects of the application of AA disorder in a symmetric manner where the disorder is introduced on the u and d sites,

$$\zeta_k^u = \zeta_k^d \quad \text{and} \quad \zeta_k^c = 0, \quad (15)$$

in the presence of interactions. We first look at the eigenvalue and eigenvector properties of this Hamiltonian, and then see how these properties are reflected in a nonequilibrium dynamical setting.

A. Statics

We start by investigating the level spacing distributions $P(s)$. To do this, the energy levels are arranged in ascending order, and the consecutive spacings are obtained as $s_i = E_{i+1} - E_i$. A large collection of such spacings is obtained with the aid of several disorder realizations. Next, the s_i are unfolded [53] by dividing the original level spacings by the mean level-spacing of the spectrum. We then study the distribution of these scaled spacings. It is well known [54] that when the states involved are localized, the probability distribution of the level spacings is Poissonian: $P(s) = e^{-s}$. On the other hand, for delocalized states, the probability distribution of the level spacings is Wigner-Dyson: $P(s) = \frac{\pi}{2} s e^{-\frac{\pi}{4}s^2}$ (GOE [54]).

In the disorder-free case, the single-particle ABF diamond lattice possesses massive degeneracy with only three energy levels. When interactions are turned on for the disorder-free model, we observe quasidegeneracy as well as a large number of gaps in the spectrum. On the application of disorder, while degenerate bands are observed in the absence of interactions in the low disorder limit, many smaller bands are observed when the interactions are also turned on. In the case of high disorder, both in the presence and absence of interactions, the spectrum displays quasidegeneracy and many smaller gaps, a behavior typically observed in quasiperiodic systems [55]. This makes the level spacing distribution not a reliable tool for studying localization characteristics [56] in the low and high disorder regime. In the intermediate disorder regime, these effects are minimized due to the interplay of flat bands and disorder. Figure 8 shows the probability distribution of the level spacing at interaction strength $V = 1$ for a fixed filling fraction $\nu = 1/3$ and different disorder strengths λ . We observe that the spacing distribution is neither GOE nor does it show a perfect fit to the Poisson distribution both at $\lambda = 0.01$ [see Fig. 8(a)] and at $\lambda = 1$ [see Fig. 8(b)]. The states are

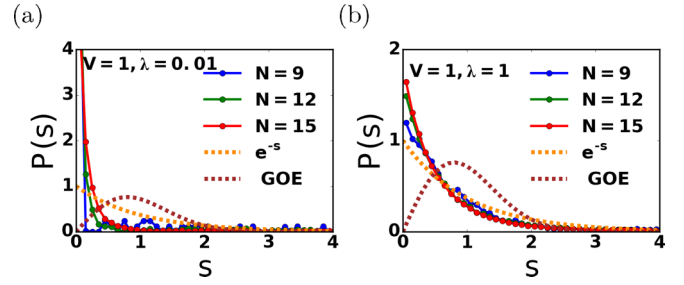


FIG. 8. In the symmetric case, level spacing distribution $P(s)$ with spacings s at interaction strength $V = 1$ for filling fraction $\nu = 1/3$ at disorder strength (a) $\lambda = 0.01$ and (b) $\lambda = 1$. The number of disorder realizations is 50 for $N = 15$ and 200 for $N = 9$ and $N = 12$.

neither ergodic nor localized in the low and intermediate disorder regimes.

As discussed above, quasidegeneracy and gaps in the low and high disorder limits yield inconclusive results when we study eigenvalue properties. We will now discuss MIPR at a fixed interaction strength $V = 1$ and various disorder strengths λ as shown in Fig. 9. For a fixed filling fraction $\nu = 1/3$, we extract the exponent γ by averaging the MIPR over the states belonging to the energy window $[\varepsilon - 0.01, \varepsilon + 0.01]$, where $\varepsilon = 0.1, 0.2 \dots 0.9$. In the low disorder regime $\lambda = 0.01$ [see Fig. 9(a)], $\gamma \approx 0.6$ over the entire energy spectrum indicating a nonergodic phase. We observe similar nonergodic behavior in the intermediate regime $\lambda = 1$ as shown in Fig. 9(b). However, in the high disorder regime with $\lambda = 100$ [see Fig. 9(c)], the exponent has a significantly lower value $\gamma \approx 0.1$, which is a signature of MBL-like behavior. In Fig. 10, we have plotted the exponent γ at different disorder strengths and observe that it shows consistent behavior over the entire spectrum.

We also study the OPDM here, with the help of the occupation spectrum $\langle n_\alpha \rangle$ at different disorder strengths $\lambda = 0.01, 1$, and 100 [see Figs. 11(a)–11(c)] and over a specific energy window $\varepsilon = [0.54, 0.57]$. At low and intermediate disorder strengths, the occupation spectrum falls monotonically with practically no dependence on system size and with no signature of the thermal value $\langle n_\alpha \rangle = \nu = 1/3$; it also does not quite reach close to 0 or 1 either indicating nonergodic behavior. However, in the high disorder regime, $\lambda = 100$, it reaches close to 0 and 1, indicating localized behavior of the single-particle states and hence an MBL-like phase. The OPDM entropy S_o is also consistent with the above inferences. While it is quite far from its thermal value [represented by dashed lines in Fig. 11(d)] in the low and intermediate disorder regimes, it shows system size independence and goes close to 0 in the MBL-like phase.

B. Nonequilibrium dynamics

Next, we study the many-body nonequilibrium dynamics with the help of particle density, entanglement entropy and return probability. For the initial state given by Eq. (13), we observe the evolution of the particle density that the CLSs corresponding to distinct particles remain isolated and unaffected by the interaction strength V as shown in Figs. 12(a)–12(c)

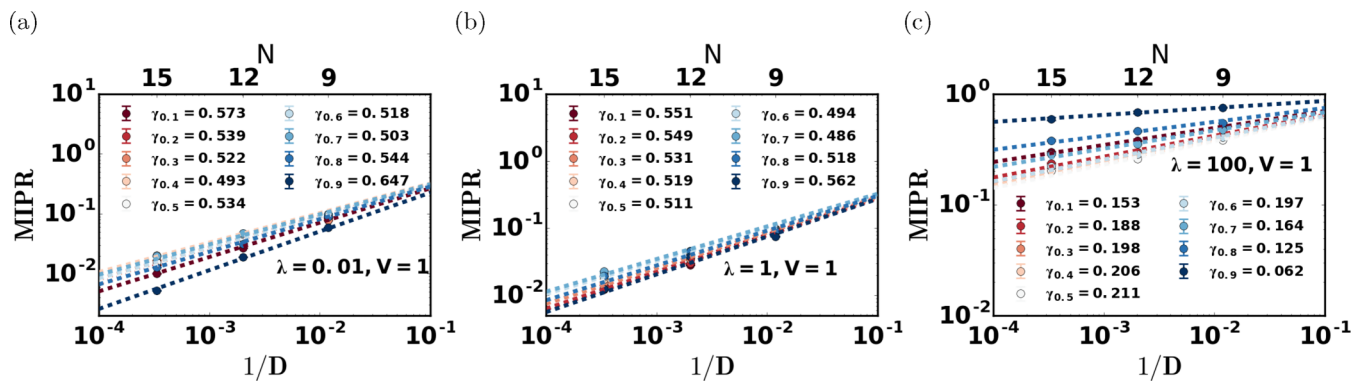


FIG. 9. In the symmetric case, MIPR averaged over states in the energy window $[\varepsilon - 0.01, \varepsilon + 0.01]$ with $1/D$ (D is the dimension of the Hilbert space), where $\varepsilon = 0.1, 0.2, \dots, 0.9$ for a fixed interaction strength $V = 1$ and disorder strength (a) $\lambda = 0.01$, (b) $\lambda = 1$, and (c) $\lambda = 100$. Number of disorder realizations are 400, 200, and 50 for system sizes $N = 9, 12$, and 15 , respectively and the filling fraction is $\nu = 1/3$.

for disorder strengths $\lambda = 0.01, 1$, and 100 , which results in caging. For the initial state given by Eq. (14), the amplitude corresponding to different CLSs overlap, and the interaction comes into play. From the time evolution of the particle density [see Figs. 12(d)–12(f)], we observe that the compact localized nature is no longer sustained. While nonergodic behavior is observed at low and intermediate disorder, at higher disorder strength ($\lambda = 100$), it is comparatively less nonergodic in the long-time limit.

We also study the entanglement entropy and return probability dynamics for both the initial configurations as shown in Fig. 13. In the case of the initial state corresponding to Eq. (13), for a subsystem of size $N_A = 1/3$, we observe that at all disorder strengths, $S_A \approx 0$ [see Fig. 13(a)], which supports the observation of caging from the particle density. From the return probability dynamics [see Fig. 13(b)], with increasing disorder strengths, and for $V = 1$, we observe that while in the low and intermediate disorder regimes, $R(t)$ has a finite value, in the higher disorder regime, it approaches unity. For the second initial state [Eq. (14)], in the low and intermediate disorder regimes after the transient, we observe a subdiffusive regime, followed by S_A reaching saturation at a value of the order of the thermal value as shown in Fig. 13(c). In the high disorder regime, we observe a logarithmically slow growth, which eventually saturates to a subthermal value. The same

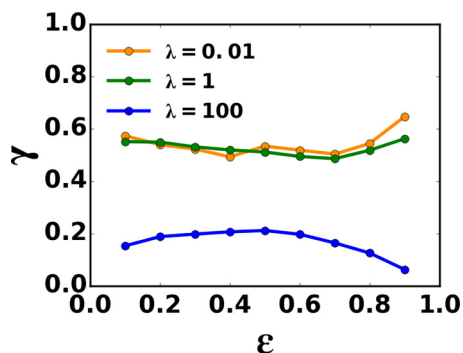


FIG. 10. The exponent γ extracted from the energy resolved MIPR in Fig. 9 with rescaled energy ε at interaction strength $V = 1$ and disorder strength $\lambda = 0.01, 1$, and 100 .

can be observed from the evolution of return probability [see Fig. 13(d)]. The dynamics of return probability supports the results observed from the particle density [see Figs. 12(d)–12(f)] and entanglement entropy with $R(t)$ close to 0 in the low and intermediate disorder regimes and with a finite magnitude in the high disorder regime.

In Fig. 14, we study the dynamics when the initial state is of the density wave type with particles on c sites of every unit cell, i.e., with filling fraction $\nu = 1/3$,

$$|\psi_{\text{in}}\rangle = \prod_{i=1}^{N/3} \hat{c}_i^\dagger |0\rangle. \quad (16)$$

The evolution of the particle density for the interaction strength $V = 1$ and disorder strengths $\lambda = 1$ and 100 , is

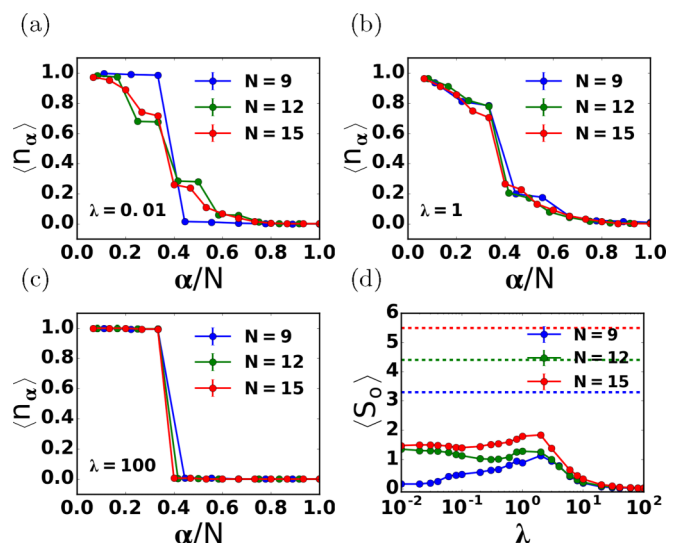


FIG. 11. Occupation spectrum $\langle n_\alpha \rangle$ with scaled index α/N at fixed interaction strength $V = 1$ and disorder strengths (a) $\lambda = 0.01$, (b) $\lambda = 1$, and (c) $\lambda = 100$, for different system sizes $N = 9, 12, 15$ and fixed filling fraction $\nu = 1/3$. (d) The average OPDM entropy S_o with increasing strength of disorder λ . Dashed lines denote the maximal value of S_o . Averaging has been performed over the eigenstates in the energy window $\varepsilon = [0.54, 0.57]$ and using 400, 200, and 50 disorder realizations for system sizes $N = 9, 12$, and 15 respectively.

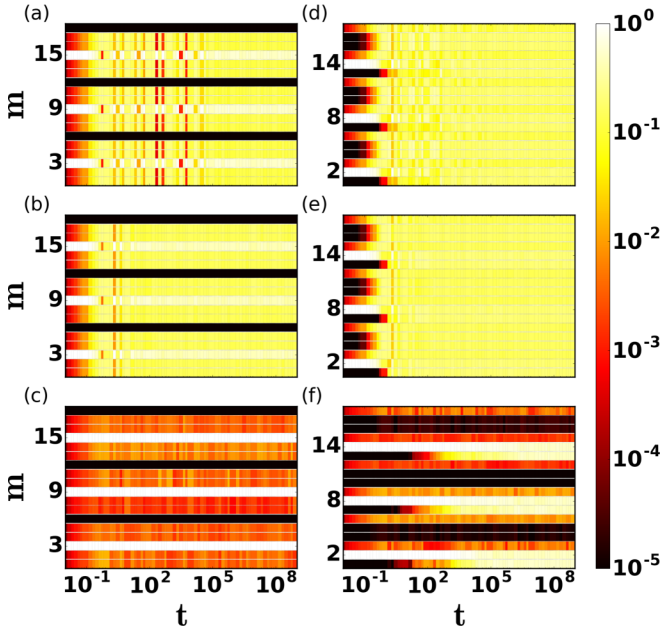


FIG. 12. In the symmetric case, particle density (whose value is represented by a color according to the code shown) as a function of time t , where m is the site index, for the initial state given by Eq. (13) for interaction strength $V = 1$ and increasing disorder strengths (a) $\lambda = 0.01$, (b) $\lambda = 1$, and (c) $\lambda = 100$. Corresponding plots show the evolution of the particle density [(d)–(f)] for the initial state given by Eq. (14). $N = 18$, $\nu = 1/6$ and 100 disorder realizations have been considered for all cases.

shown in Figs. 14(a) and 14(b). While at low (not shown here) and intermediate disorder, we observe that the particle density spreads uniformly over all the sites, at high disorder strength

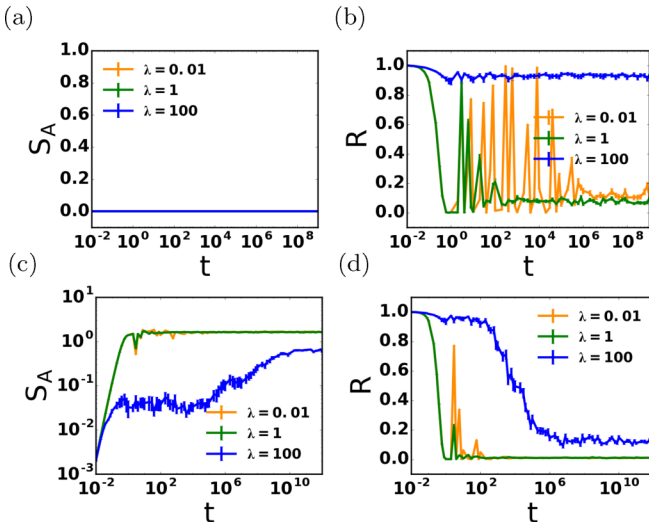


FIG. 13. In the symmetric case, (a) entanglement entropy S_A for a subsystem of size $N_A = N/3$ and (b) return probability R as a function of time t for the initial state given by Eq. (13). (c) Entanglement entropy S_A for a subsystem of size $N_A = N/3$ and (d) return probability R as a function of time t for the initial state given by Eq. (14). The interaction strength is fixed as $V = 1$ with increasing disorder strengths λ . For all plots, $N = 18$, $\nu = 1/6$ and number of disorder realizations is 100.

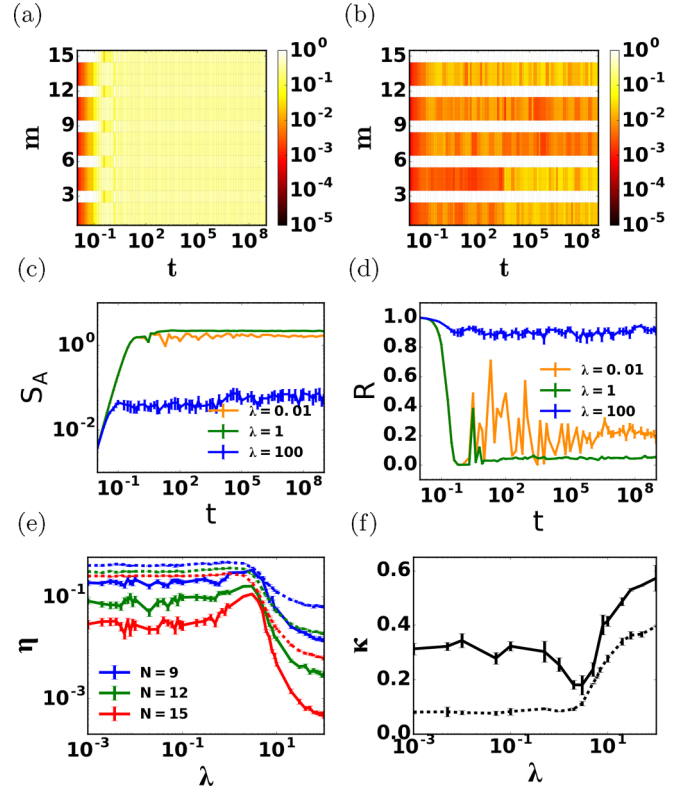


FIG. 14. The particle density (whose value is represented by a color according to the code shown) as a function of time t , where m is the site index for the initial state given by Eq. (16) and for disorder strengths (a) $\lambda = 1$ and (b) $\lambda = 100$. (c) Entanglement entropy S_A for a subsystem of size $N_A = N/3$ and (d) return probability R as a function of time t . Here the interaction strength is fixed to $V = 1$, and the system size is $N = 15$, with filling fraction $\nu = 1/3$ and averaging has been done over 50 disorder realizations. (e) In the long-time limit $t = 10^9$, the NPR η as a function of disorder strength λ for various system sizes N , solid lines correspond to the initial state given by Eq. (16) while dashed lines correspond to the initial state given by Eq. (17). (f) The scaling exponent κ as a function of disorder strength λ . Here $V = 1$ and $\nu = 1/3$, and the number of disorder realizations are at least 50 for all the system sizes.

$\lambda = 100$, the particle density is significantly localized over the initially occupied sites, indicating MBL-like behavior. We also study the dynamics of entanglement entropy S_A as shown in Fig. 14(c) at $V = 1$. After the initial transient, S_A shows a subdiffusive growth in the low and intermediate disorder regimes and saturates to a large value indicating delocalization in the many-body system. The high disorder regime shows a logarithmic growth with time t , saturating to a much lower magnitude compared to the thermal value indicating MBL-like behavior. The return probability dynamics is shown in Fig. 14(d). For low disorder, it saturates to a finite value, indicating nonergodic behavior, while in the intermediate disorder regime, the magnitude is much smaller (but $\neq 0$), indicating that the phase has a higher nonergodic tendency. At higher disorder strengths, it is close to unity, which is a signature of MBL-like behavior.

We further study the normalized participation ratio (NPR) [22], in the long-time limit ($t = 10^9$) to understand the

many-body phases. We consider two types of initial states with filling fraction $\nu = 1/3$, one given by Eq. (16) and another density wave type state with particles on d sites of every unit cell,

$$|\psi_{\text{in}}\rangle = \prod_{i=1}^{N/3} \hat{d}_i^\dagger |0\rangle. \quad (17)$$

For any time-evolved many-body state, $|\Psi(t)\rangle = \sum_{i=1}^D C_i(t)|i\rangle$, the NPR is given as

$$\eta = \frac{1}{D \sum_i |C_i|^4}.$$

In the long-time limit ($t \rightarrow \infty$), η is independent of system size N in the ergodic phase; in contrast, it decays exponentially with the system size in the localized phase [22]. In Fig. 14(e), we study the dependence of NPR η on the disorder strength λ , fixed interaction strength $V = 1$ and increasing system sizes. Here the solid lines correspond to the initial state given by Eq. (16) while the dashed lines correspond to the initial state given by Eq. (17). We observe that in both cases, η is system size dependent at all strengths of disorder λ , indicating the absence of the thermal phase. Further, the exponent κ can be extracted at various disorder strengths using the relation $\eta \propto e^{-\kappa N}$. In Fig. 14(f), we plot κ with increasing disorder strength and observe that for both initial states, in the low and intermediate disorder regime $0 < \kappa < 0.5$, indicating nonergodic behavior. However, at higher disorder strength, it reaches near 0.5, which is a sign of many-body localization [22].

For the second type of symmetric configuration, when the disorder is only considered on the c site,

$$\zeta_k^u = \zeta_k^d = 0 \quad \text{and} \quad \zeta_k^c \neq 0 \quad (18)$$

we observe that the results are qualitatively similar to the one discussed above.

VI. INTERACTIONS AND ANTISYMMETRIC DISORDER

In this section, we study the interplay of antisymmetric disorder and interactions. Specifically, we consider the antisymmetric application of the AA disorder on the u and d sites,

$$\zeta_k^u = -\zeta_k^d \quad \text{and} \quad \zeta_k^c = 0, \quad (19)$$

in the presence of interactions. We first study the eigenvalue and eigenvector properties, and then investigate them in a nonequilibrium dynamical setting as well.

A. Statics

We begin by analyzing the eigenvalue properties with the aid of the level-spacing ratio r_{av} [54], defined as

$$r_{av} = \left\langle \frac{1}{N-2} \sum_{i=1}^{N-2} \frac{\min[s_i, s_{i+1}]}{\max[s_i, s_{i+1}]} \right\rangle. \quad (20)$$

Here the energies E_i 's are first organized in ascending order, which are used to obtain the energy-level spacings $s_i = E_{i+1} - E_i$. The braces in Eq. (20) represent the average over

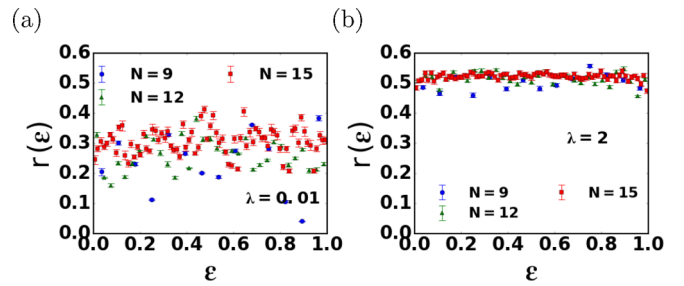


FIG. 15. In the antisymmetric case, energy-resolved gap-ratio as a function of the fractional eigenstate index ϵ for disorder strength (a) $\lambda = 0.01$ and (a) $\lambda = 2$. The number of disorder realizations is 500, 400, and 50 for system sizes $N = 9, 12$, and 15 , respectively.

disorder realizations. In the delocalized and localized phases, r_{av} is expected to be approximately 0.528 and 0.386, respectively [54]. In Fig. 15, we study the energy-resolved level spacing ratio by dividing the many-body energy spectrum into several equal segments and calculating the local average of the level-spacing ratio for each segment of the spectrum. While in the low disorder regime [see Fig. 15(a)] $r_{av} \approx 0.3$ indicating a mixed nonergodic phase, $r_{av} \approx 0.52$ for $\lambda = 2$ [see Fig. 15(b)] suggests a thermal-like phase. As discussed in Sec. V A, in the high disorder regime, the spectrum displays quasi-degeneracy and many gaps; we do not show the results here as they are inconclusive.

We next study the eigenvector properties with the help of MIPR and the OPDM. We study MIPR at a fixed interaction strength $V = 1$ and various disorder strengths λ as shown in Fig. 16. For a fixed filling fraction $\nu = 1/3$, we extract the exponent γ by averaging the MIPR over the states belonging to the energy window $[\epsilon - 0.01, \epsilon + 0.01]$, where $\epsilon = 0.1, 0.2, \dots, 0.9$. In the low disorder regime, $\lambda = 0.01$ [see Fig. 16(a)], we observe a nonergodic mixed phase owing to the spread of the exponent γ over a wide range $0.54 < \gamma < 0.80$. In the intermediate disorder case, γ has a significantly higher magnitude, which signifies thermal-like behavior [see Fig. 16(b)]. At high disorder strength $\lambda = 100$, the exponent γ has a small magnitude ≈ 0.07 over the entire spectrum indicating an MBL-like phase, as shown in Fig. 16(c). In Fig. 17, we have plotted the exponent γ at different disorder strengths and observe that in the low disorder regime, $\gamma \approx 0.8$ corresponding to the energy window about $\epsilon = 0.9$, which signifies the presence of thermal-like states that contribute to the mixed nonergodic behavior. We observe that the intermediate and high disorder regimes show thermal-like and MBL-like behavior, respectively, over the entire spectrum.

We next study the OPDM with the help of the occupation spectrum $\langle n_\alpha \rangle$ at different disorder strengths $\lambda = 0.01, 2$, and 100 [see Figs. 18(a)–18(c)] and over the energy window $\epsilon = [0.54, 0.57]$. In the intermediate regime [Fig. 18(b)], we observe that with increasing system size, $\langle n_\alpha \rangle$ spreads about the filling fraction $\nu = 1/3$ with a characteristic inverse system-size variation on either side of the critical value of the $\frac{\alpha}{N}$, indicating a thermal phase. In contrast, in the high disorder regime [Fig. 18(c)], $\langle n_\alpha \rangle$ reaches close to 0 and 1, indicating localized behavior of the single-particle states. Hence, the phase is MBL like. In the low disorder regime

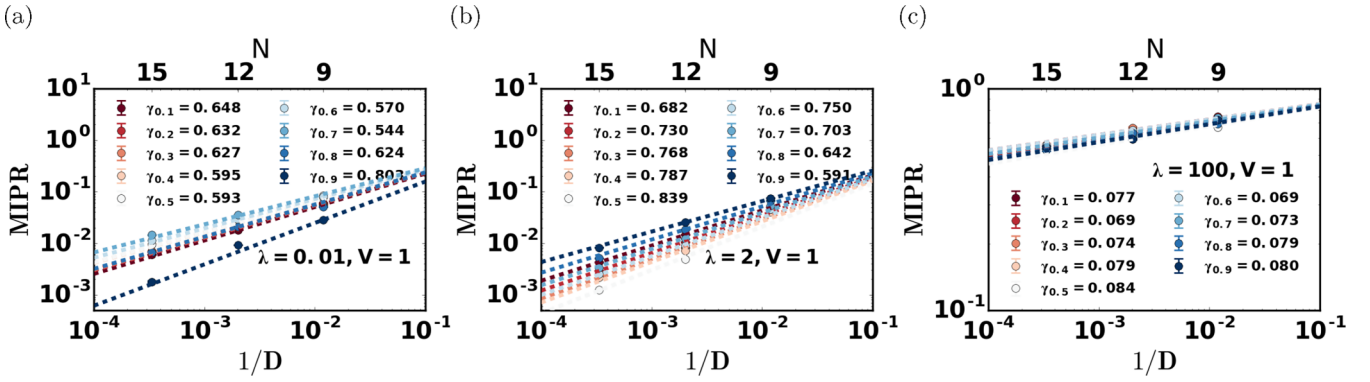


FIG. 16. In the antisymmetric case, MIPR averaged over states in the energy window $[\varepsilon - 0.01, \varepsilon + 0.01]$ with $1/D$ (D is the dimension of the Hilbert space), where $\varepsilon = 0.1, 0.2, \dots, 0.9$ for a fixed interaction strength $V = 1$ and disorder strength (a) $\lambda = 0.01$, (b) $\lambda = 2$, and (c) $\lambda = 100$. Number of disorder realizations are 400, 200, and 50 for system sizes $N = 9, 12$, and 15 , respectively and the filling fraction is $\nu = 1/3$.

[(Fig. 18(a)], the occupation spectrum is neither spread about the thermal value $\langle n_\alpha \rangle = \nu = 1/3$ nor does it reach close to 0 and 1 (like in MBL), thus indicating mixed nonergodic behavior. The OPDM entropy S_o [see in Fig. 18(d)] signifies a nonergodic phase in the low disorder regime as it neither reaches the thermal value (dashed lines) nor the MBL value (0). In the intermediate disorder case, S_o reaches its thermal value denoted by dashed lines, especially for $N = 15$, while it approaches 0 in the high disorder case, indicating MBL-like behavior.

B. Nonequilibrium dynamics

We next study many-body nonequilibrium dynamics with several measures such as particle density, entanglement entropy, and return probability. We first consider the initial state given by Eq. (13), a product state for a system size $N = 18$ and filling fraction $\nu = 1/6$, with particles occupying the c sites of alternate unit cells. From the evolution of the particle density shown in Figs. 19(a)–19(c), we observe that for all disorder strengths, the CLS-like behavior persists at early times ($t < 1$). However, for time $t > 1$, while the particle density spreads uniformly over the entire lattice in the low and intermediate disorder regimes, it shows a comparatively less ergodic behavior in the high disorder case. We also study the dynamics for the second initial state given by Eq. (14). For

low and intermediate disorder strengths [see Figs. 19(d) and 19(e)], we observe that the particle density is uniformly spread over all the sites indicating ergodic behavior. In contrast, at higher disorder strength $\lambda = 100$ [see Fig. 19(f)], the particle density is significantly localized over the initially occupied sites.

The entanglement entropy and return probability dynamics for both the initial configurations are shown in Fig. 20. In the case of the initial state corresponding to Eq. (13), S_A has near-zero magnitude at early times, as shown in Fig. 20(a). However, the low and intermediate disorder regimes saturate to a large magnitude after the initial transient. At higher disorder strengths ($\lambda = 100$), we observe that the behavior is relatively more localized with the entanglement entropy S_A

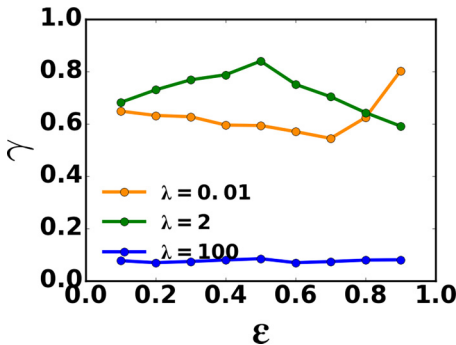


FIG. 17. The exponent γ extracted from the energy resolved MIPR in Fig. 16 with rescaled energy ε at interaction strength $V = 1$ and disorder strength $\lambda = 0.01, 2$, and 100 .

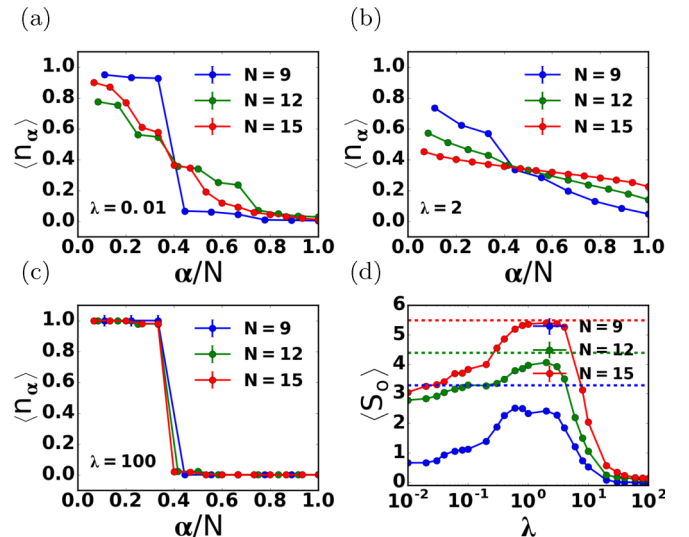


FIG. 18. Occupation spectrum $\langle n_\alpha \rangle$ with scaled index α/N at fixed interaction strengths $V = 1$ and disorder strengths (a) $\lambda = 0.01$, (b) $\lambda = 2$, and (c) $\lambda = 100$, for different system sizes $N = 9, 12, 15$ and fixed filling fraction $\nu = 1/3$. (d) The average OPDM entropy S_o with increasing strength of disorder λ . Dashed lines denote the maximal value of S_o . Averaging has been performed over the eigenstates in the energy window $\varepsilon = [0.54, 0.57]$ and using 400,200, and 50 disorder realizations for system sizes $N = 9, 12$, and 15 , respectively.

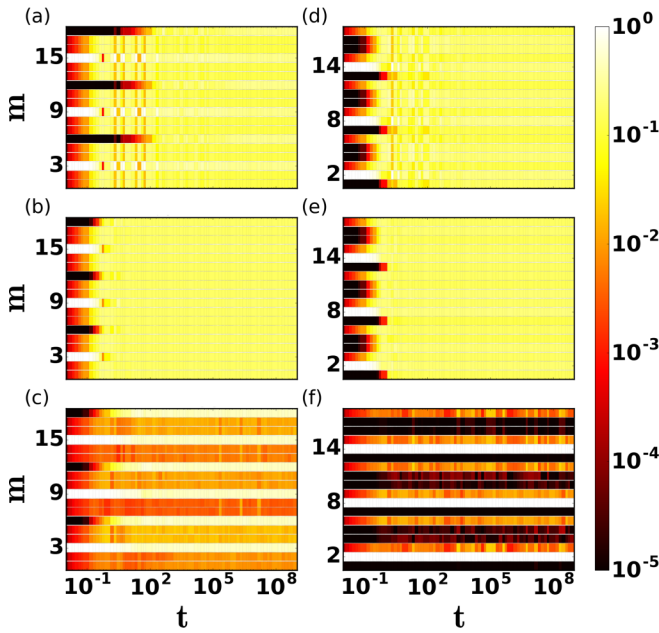


FIG. 19. In the antisymmetric case, particle density (whose value is represented by a color according to the code shown) as a function of time t , where m is the site index, for the initial state given by Eq. (13) for interaction strength $V = 1$ and increasing disorder strengths (a) $\lambda = 0.01$, (b) $\lambda = 2$, and (c) $\lambda = 100$. Corresponding plots [(d)–(f)] show the evolution of the particle density for the initial state given by Eq. (14). $N = 18$, $\nu = 1/6$ and 100 disorder realizations have been considered for all cases.

[see Fig. 20(a)] saturating to a lower magnitude. From the return probability dynamics as shown in Fig. 20(b), while

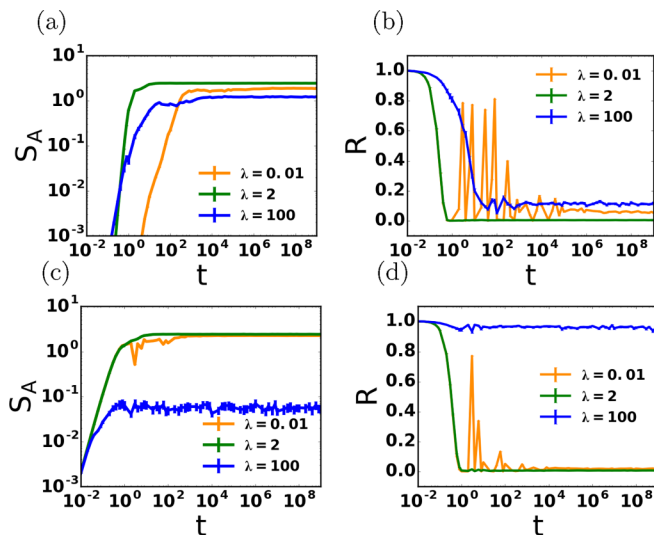


FIG. 20. In the antisymmetric case, (a) the entanglement entropy S_A for a subsystem of size $N_A = N/3$ and (b) return probability R as a function of time t for the initial state given by Eq. (13). (c) Entanglement entropy S_A for a subsystem of size $N_A = N/3$ and (d) return probability R as a function of time t for the initial state given by Eq. (14). The interaction strength is fixed as $V = 1$ for various disorder strengths λ . For all plots, $N = 18$, $\nu = 1/6$, and the number of disorder realizations is 100.

for low and high disorder $R(t)$ saturates to a finite value indicating nonergodic behavior, in the intermediate disorder regime, $R(t) \approx 0$, which signifies a thermal-like phase. For the second initial state given by Eq. (14), after the initial transient, in the low disorder regime, we observe oscillatory behavior followed by a subdiffusive growth after which S_A saturates near the thermal value [see Fig. 20(c)]. The behavior of S_A in the intermediate disorder regime is similar to the low disorder case, except that the oscillatory part is absent. After the transient, there is a subdiffusive increment in S_A , which saturates to a large value indicating delocalization in the many-body system. In contrast, in the high disorder region, it saturates to a low value signifying MBL. We also study the evolution of the return probability, as shown in Fig. 20(d). In the long-time limit, it saturates to 0 in the low and intermediate disorder regimes indicating thermal-like behavior. At the same time, it is close to 1 in the high disorder regime, which is a signature of many-body localization.

We next study the nonequilibrium dynamics of the system for the two initial states by considering filling fraction $\nu = 1/3$. The evolution of the particle density is shown in Figs. 21(a) and 21(b), at the interaction strength $V = 1$ and for disorder strengths $\lambda = 2$ and 100. We observe mixed nonergodic behavior at low disorder strength (not shown here). In contrast, we see ergodic behavior at intermediate disorder strengths, with the particle density spread uniformly over all the sites. At high disorder strength $\lambda = 100$, the particle density is significantly localized over the initially occupied sites. We also study the dynamics of entanglement entropy S_A as shown in Fig. 21(c) at $V = 1$. After the initial transient, S_A shows a subdiffusive growth in both the low and intermediate disorder regimes; however, it saturates to a large value for $\lambda = 2$, indicating an ergodic phase, while for $\lambda = 0.01$, it saturates to a comparatively lower value indicating weak delocalization in the system. In the high disorder case, after the initial transient, S_A saturates to a sub-thermal value indicating localization. From the dynamics of the return probability [see Fig. 21(d)], we observe that it saturates to a finite value in the low and high disorder phases. In contrast, it saturates close to 0 in the intermediate phase indicating thermal behavior.

We next study the NPR [22] in the long-time limit for the initial states given by Eq. (16) (solid lines) and Eq. (17) (dashed lines) as shown in Fig. 21(e). In the case of the initial state given by Eq. (16), while η is system size dependent in the low and high disorder regimes, it shows system size independence in the intermediate disorder case. We then extract the exponent κ and plot it as a function of disorder strength λ in Fig. 21(f). In the low disorder case, κ lies between 0 and 0.5, indicating nonergodic behavior while in the intermediate regime $\kappa = 0$, indicating a thermal phase. In contrast, in the high disorder regime, we observe $\kappa \approx 0.5$, which is a signature of many-body localization. For the other initial state given by Eq. (17), in the low disorder regime, η tends to be system size-independent [see Fig. 21(e)], with κ close to 0 [Fig. 21(f)], which indicates that it is close to the ergodic phase. In the intermediate regime, the phase is thermal as η is system size independent and $\kappa = 0$. In the higher disorder regime, η is system size dependent with κ close to 0.5, indicating an MBL-like phase.

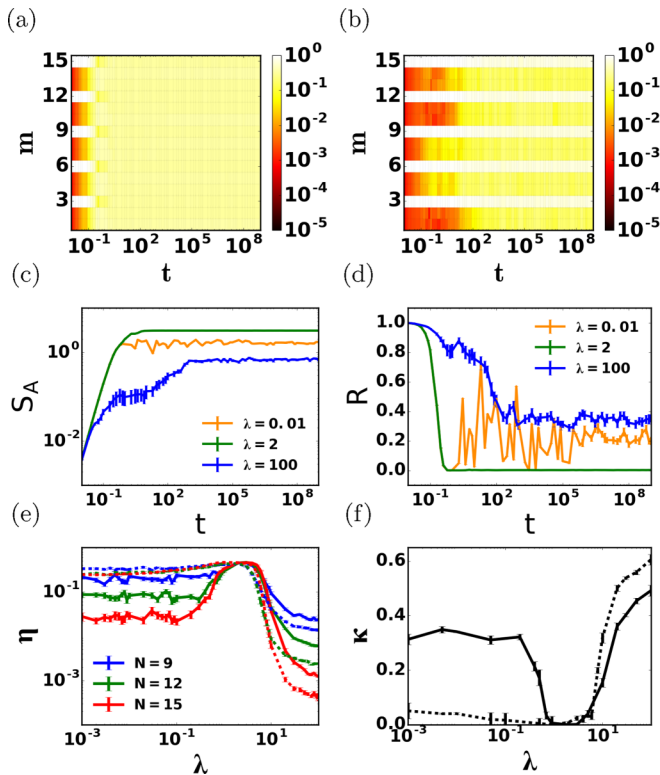


FIG. 21. The particle density (whose value is represented by a color according to the code shown) as a function of time t , where m is the site index for the initial state given by Eq. (16) for disorder strengths (a) $\lambda = 2$ and (b) $\lambda = 100$. (c) Entanglement entropy S_A for a subsystem of size $N_A = N/3$ and (d) return probability R as a function of time t . Here the interaction strength is fixed to $V = 1$, and the system size is $N = 15$ with filling fraction $\nu = 1/3$, and averaging has been done over 50 disorder realizations. (e) In the long-time limit $t = 10^9$, NPR η as a function of disorder strength λ for various system sizes N , solid lines correspond to initial state given by Eq. (16) while dashed lines correspond to initial state given by Eq. (17). (f) The scaling exponent κ as a function of disorder strength λ . Here $V = 1$ and $\nu = 1/3$, and the number of disorder realizations is at least 50 for all the system sizes.

VII. CONCLUSION

In this paper, we have systematically investigated the single-particle dynamics and the interplay of many-body interactions and quasiperiodic AA disorder in the one-dimensional ABF diamond lattice. We find that the compact localized states observed for the clean system and when the disorder is applied symmetrically in the single particle case [37] sustain quantum caging even in a nonequilibrium dynamical set-up. In contrast, in the long-time limit, the wave function spreads over the entire lattice in the presence of antisymmetric disorder. This can be attributed to the loss of compact localization and the presence of multifractal eigenstates in the static case [37].

In the presence of interactions and zero disorder in the system, nonergodic phases are observed at all interaction strengths. In general, nonequilibrium dynamics support the findings from the static case. However, the many-body system manifests quantum caging for specially engineered initial

states. When our interacting many-body system is subjected to symmetric disorder, nonergodic phases are observed at low and intermediate disorder strengths. In contrast, an MBL-like phase is observed at higher disorder strengths. Studying nonequilibrium dynamics, we find nonergodic regimes in the case of low and intermediate disorder strengths, while localization characteristics dominate in the high disorder case. Quantum caging behavior is supported for specific initial configurations, independent of the strength of interaction or disorder.

The antisymmetric application of disorder in the presence of interactions in the system result in three distinct phases: A nonergodic mixed phase at low disorder strengths, a thermal phase at intermediate disorder strengths, and an MBL-like phase at higher strengths of disorder. Even in the mixed nonergodic phase, some states show thermal-like behavior. A study of the nonequilibrium dynamics shows that for different initial states, in the low disorder regime, a mixed phase exists with a varying magnitude of nonergodicity; for the intermediate disorder, the phase is always thermal. In the high disorder case, the phase shows varying magnitudes of nonergodicity, inclined towards many-body localization.

We also want to remark on the case when the on-site disorder is chosen from a uniform uncorrelated random distribution in the presence of interactions. Interestingly, for both the symmetric and antisymmetric cases, the resulting phase is similar in the low, intermediate, and high disorder strengths to those obtained when applying the quasiperiodic disorder. We conclude that the observed many-body phases are due to the symmetry of the applied disorder as reported previously in the single particle case [37]. Also, in the antisymmetric case, the presence of mixed nonergodic, thermal and MBL-like phases at the low, intermediate and high disorder strengths, respectively, is qualitatively similar to phases that emerge as a result of the application of the uniform disorder on all sites as reported in [32].

Thus, our paper shows that the interplay of quasiperiodic disorder, interactions and flat-band structure in the diamond lattice results in an exciting phase diagram. Exploring distinctive phases in other interacting and disordered flat-band systems would be an interesting direction for further research. With the recent surge in the experimental study of engineered flat-band systems, such phases could be realized in optical lattices for cold atoms.

ACKNOWLEDGMENTS

We are grateful to Ajith Ramachandran for the careful reading of the manuscript and discussions. We are grateful to the High-Performance Computing (HPC) facility at IISER Bhopal, where large-scale computations of this project were run. A.A. is grateful to the Council of Scientific and Industrial Research (CSIR), India, for her Ph.D. fellowship. N.R. acknowledges support from the Indian Institute of Science under the IoE-IISc fellowship program. A.S. acknowledges financial support from SERB via the Grant No CRG/2019/003447 and DST via the DST-INSPIRE Faculty Award No. DST/INSPIRE/04/2014/002461.

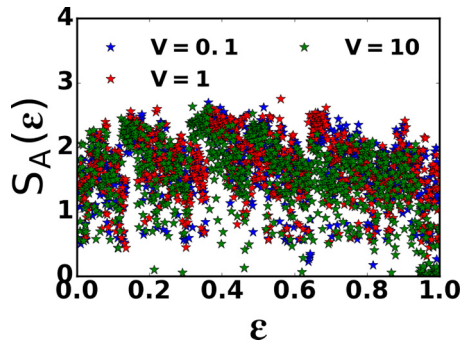


FIG. 22. The half-chain entanglement entropy $S_A(\epsilon)$ of all the eigenstates as a function of the fractional eigenstate index ϵ for $N = 18$ with $\nu = 1/6$ for interaction strengths $V = 0.1, 1$, and 10 .

APPENDIX: ENTANGLEMENT ENTROPY

In this section, we analyze the effect of interactions on the ABF diamond lattice by calculating the half-chain entanglement entropy S_A of all the many-body eigenstates. We first discuss the case when interactions are turned on in the disorder-free model, and then consider cases where disorder is applied in a symmetric and antisymmetric manner in the presence of interactions.

Figure 22 shows the half-chain entanglement entropy S_A of all the many-body eigenstates at various interaction strengths V for a system size $N = 18$ and filling fraction $\nu = 1/6$. For all interaction strengths, $V = 0.1, 1$, and 10 , while a significant fraction of the eigenstates shows a large magnitude of the entanglement entropy, it does not vary smoothly with

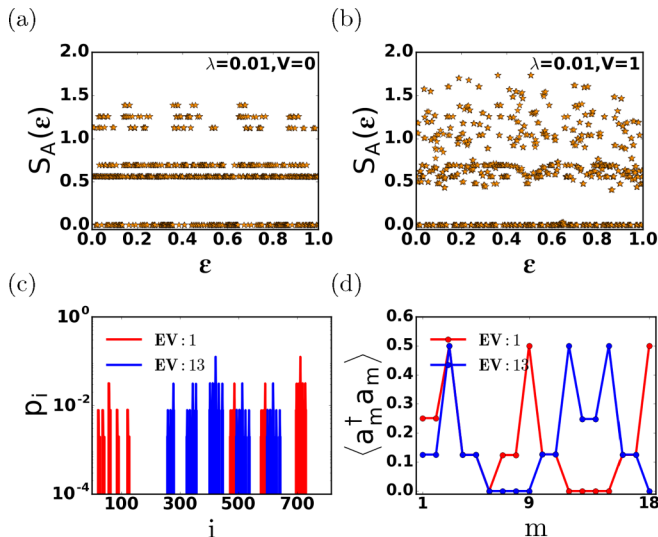


FIG. 23. The half-chain entanglement entropy $S_A(\epsilon)$ for all the eigenstates as a function of the fractional eigenstate index ϵ for disorder strength $\lambda = 0.01$ and interaction strengths (a) $V = 0$ and (b) $V = 1$. (c) The wavefunction probability of two states indexed as $EV : 1$ with $S_A \neq 0$ and $EV : 13$ with $S_A = 0$. Here $i = 1, \dots, D$, where D is the dimension of the particle number constraint Hilbert space. (d) The corresponding particle density $\langle a_m^\dagger a_m \rangle$, where m is site index at $V = 0$. For all the cases, $N = 18$, filling fraction $\nu = 1/6$ and single-disorder realization has been considered.

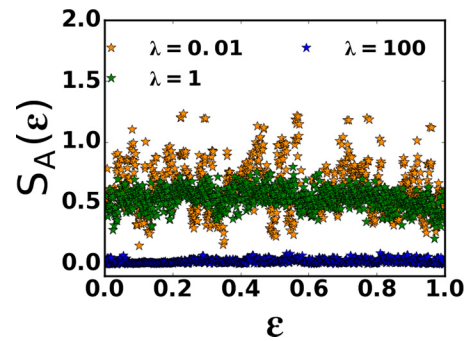


FIG. 24. In the symmetric case, half-chain entanglement entropy $S_A(\epsilon)$ for all the eigenstates as a function of the fractional eigenstate index ϵ for disorder strengths $\lambda = 0.01, 1$, and 100 . The averaging has been performed over 50 disorder realizations.

the fractional eigenstate index ϵ . This indicates the presence of a nonergodic phase, which agrees with the MIPR and OPDM results shown in Sec. IV.

Next, we study the application of symmetric disorder; we have reported the presence of compactly localized states [37] in the single-particle case. Interestingly, in the case of noninteracting fermions, from the half-chain entanglement entropy, we observe that the eigenstates can be broadly divided into two categories [see Fig. 23(a)], one with $S_A \neq 0$

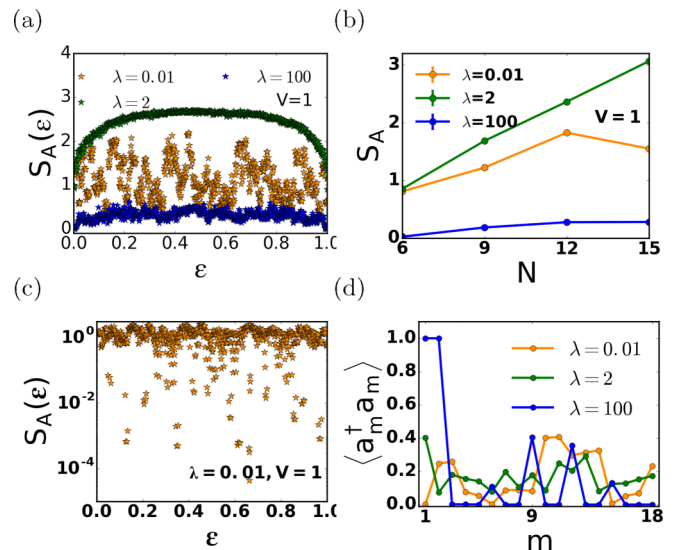


FIG. 25. (a) The half-chain entanglement entropy $S_A(\epsilon)$ of all the eigenstates as a function of the fractional eigenstate index ϵ for $N = 18$ with $\nu = 1/6$ for various disorder strengths λ and fixed interaction strength $V = 1$. Here averaging has been performed over 100 disorder realizations. (b) Entanglement entropy S_A averaged over the eigenstates in the energy window $\epsilon = [0.54, 0.57]$ with system size N , filling fraction $\nu = 1/3$ and subsystem size $N_A = N/3$. Here interaction strength $V = 1$ and disorder realizations is 100. (c) The half-chain entanglement entropy $S_A(\epsilon)$ of all the eigenstates as a function of the fractional eigenstate index ϵ for $N = 18$, filling fraction $\nu = 1/6$, disorder strength $\lambda = 0.01$, interaction strength $V = 1$ and single disorder realization. (d) Particle density $\langle a_m^\dagger a_m \rangle$ with site index m , filling fraction $\nu = 1/3$ for the infinite temperature state at $\theta = 0$ and $V = 1$.

and the other with $S_A = 0$. We choose a state corresponding to $S_A \neq 0$ with index $EV = 1$ and another corresponding to $S_A = 0$, with index $EV = 13$. In Fig. 23(c), we have plotted both eigenstates in the particle number-constrained space with the index i running over $1, 2, \dots, D$ and observe nonzero amplitude only on a finite number of sites. For the given state, we calculate the particle density $\langle a_j^\dagger a_j \rangle$ [see Eq. (9)] on all the sites $j = 1, 2, \dots, N$ as shown in Fig. 23(d). In the case of the state corresponding to $S_A = 0$, the particle density is zero both at the subsystem boundary ($N/2$ or $N/2 + 1$) as well as the system boundaries (1 or N) as periodic boundary conditions have been considered thereby disassociating the two subsystems. However, the same is not true for the states where the entanglement is nonzero. This effect persists for all strengths of the disorder as well as on the introduction of interactions [see Fig. 23(b)]. We conclude that this is a many-body effect in a disordered system hosting compactly localized states. Also, a blind disorder averaging the entanglement entropy would wash out this behavior, as shown in Fig. 24.

Figure 25(a) shows the half-chain entanglement entropy for all the many-body eigenstates in the case of antisymmetric application of disorder and interaction strength $V = 1$. In the low disorder case, S_A shows both rises and dips, indicating the presence of a nonergodic mixed phase. In the intermediate

disorder regime, S_A has a smooth dependence on the eigenstates with a large magnitude indicating thermal behavior. In contrast, for the higher disorder $\lambda = 100$, we observe S_A with a meagre value indicating MBL-like behavior. These results agree with those discussed in Sec. VI from the study of MIPR and OPDM. In Fig. 25(b), we plot the entanglement entropy S_A for a fixed filling fraction $\nu = 1/3$ and subsystem size $N_A = 1/3$ with increasing system size N in the energy window $\varepsilon = [0.54, 0.57]$ [57]. We find that the intermediate disorder case ($\lambda = 2$) follows a volume-law scaling while an area-law-like behavior is seen in the high disorder regime ($\lambda = 100$). In the low disorder regime, S_A initially increases and eventually saturates as a function of system size, thus indicating nonergodic behavior. We also study a single disorder realization of the half-chain entanglement entropy with $\lambda = 0.01$ and $V = 1$ [see Fig. 25(c)]. Unlike the symmetric disorder case, we observe that $S_A \neq 0$ for any eigenstate. We also study the particle density [see Fig. 25(d)] for the infinite temperature state and observe that in the low disorder case ($\lambda = 0.01$), it is unevenly spread over the lattice sites indicating nonergodic behavior. In contrast, at $\lambda = 2$, it spreads out uniformly, showing thermal behavior, and at higher disorder strengths $\lambda = 100$, it is localized over a few sites.

-
- [1] W. Maimaiti, A. Andreanov, H. C. Park, O. Gendelman, and S. Flach, Compact localized states and flat-band generators in one dimension, *Phys. Rev. B* **95**, 115135 (2017).
- [2] P. Sathé, F. Harper, and R. Roy, Compactly supported Wannier functions and strictly local projectors, *J. Phys. A: Math. Theor.* **54**, 335302 (2021).
- [3] S. A. Parameswaran, R. Roy, and S. L. Sondhi, Fractional quantum Hall physics in topological flat bands, *C. R. Phys.* **14**, 816 (2013).
- [4] E. J. Bergholtz and Z. Liu, Topological flat band models and fractional Chern insulators, *Int. J. Mod. Phys. B* **27**, 1330017 (2013).
- [5] O. Derzhko, J. Richter, and M. Maksymenko, Strongly correlated flat-band systems: The route from Heisenberg spins to Hubbard electrons, *Int. J. Mod. Phys. B* **29**, 1530007 (2015).
- [6] S. Flach, D. Leykam, J. D. Bodyfelt, P. Matthies, and A. S. Desyatnikov, Detangling flat bands into Fano lattices, *Europhys. Lett.* **105**, 30001 (2014).
- [7] D. Leykam, A. Andreanov, and S. Flach, Artificial flat band systems: From lattice models to experiments, *Adv. Phys.: X* **3**, 1473052 (2018).
- [8] J. Vidal, B. Douçot, R. Mosseri, and P. Butaud, Interaction Induced Delocalization for Two Particles in a Periodic Potential, *Phys. Rev. Lett.* **85**, 3906 (2000).
- [9] B. Douçot and J. Vidal, Pairing of Cooper Pairs in a Fully Frustrated Josephson-Junction Chain, *Phys. Rev. Lett.* **88**, 227005 (2002).
- [10] J. Vidal, R. Mosseri, and B. Douçot, Aharonov-Bohm Cages in Two-Dimensional Structures, *Phys. Rev. Lett.* **81**, 5888 (1998).
- [11] J. Vidal, P. Butaud, B. Douçot, and R. Mosseri, Disorder and interactions in Aharonov-Bohm cages, *Phys. Rev. B* **64**, 155306 (2001).
- [12] F. Evers and A. D. Mirlin, Anderson transitions, *Rev. Mod. Phys.* **80**, 1355 (2008).
- [13] L. Fleishman and P. W. Anderson, Interactions and the Anderson transition, *Phys. Rev. B* **21**, 2366 (1980).
- [14] B. L. Altshuler, Y. Gefen, A. Kamenev, and L. S. Levitov, Quasiparticle Lifetime in a Finite System: A Nonperturbative Approach, *Phys. Rev. Lett.* **78**, 2803 (1997).
- [15] P. Jacquod and D. L. Shepelyansky, Emergence of Quantum Chaos in Finite Interacting Fermi Systems, *Phys. Rev. Lett.* **79**, 1837 (1997).
- [16] D. Basko, I. Aleiner, and B. Altshuler, Metal-insulator transition in a weakly interacting many-electron system with localized single-particle states, *Ann. Phys.* **321**, 1126 (2006).
- [17] A. Polkovnikov, K. Sengupta, A. Silva, and M. Vengalattore, Colloquium: Nonequilibrium dynamics of closed interacting quantum systems, *Rev. Mod. Phys.* **83**, 863 (2011).
- [18] A. Ahmed, N. Roy, and A. Sharma, Dynamics of spectral correlations in the entanglement Hamiltonian of the Aubry-André-Harper model, *Phys. Rev. B* **104**, 155137 (2021).
- [19] D. A. Abanin, E. Altman, I. Bloch, and M. Serbyn, Colloquium: Many-body localization, thermalization, and entanglement, *Rev. Mod. Phys.* **91**, 021001 (2019).
- [20] A. Pal and D. A. Huse, Many-body localization phase transition, *Phys. Rev. B* **82**, 174411 (2010).
- [21] R. Nandkishore and D. A. Huse, Many-body localization and thermalization in quantum statistical mechanics, *Annu. Rev. Condens. Matter Phys.* **6**, 15 (2015).
- [22] S. Iyer, V. Oganesyan, G. Refael, and D. A. Huse, Many-body localization in a quasiperiodic system, *Phys. Rev. B* **87**, 134202 (2013).
- [23] M. Schiulaz, A. Silva, and M. Müller, Dynamics in many-body localized quantum systems without disorder, *Phys. Rev. B* **91**, 184202 (2015).

- [24] M. van Horssen, E. Levi, and J. P. Garrahan, Dynamics of many-body localization in a translation-invariant quantum glass model, *Phys. Rev. B* **92**, 100305(R) (2015).
- [25] R. Mondaini and Z. Cai, Many-body self-localization in a translation-invariant Hamiltonian, *Phys. Rev. B* **96**, 035153 (2017).
- [26] S. Tilleke, M. Daumann, and T. Dahm, Nearest neighbour particle-particle interaction in fermionic quasi one-dimensional flat band lattices, *Z. Naturforsch. A* **75**, 393 (2020).
- [27] C. Danieli, A. Andreanov, and S. Flach, Many-body flatband localization, *Phys. Rev. B* **102**, 041116(R) (2020).
- [28] T. Orito, Y. Kuno, and I. Ichinose, Nonthermalized dynamics of flat-band many-body localization, *Phys. Rev. B* **103**, L060301 (2021).
- [29] C. Danieli, A. Andreanov, T. Mithun, and S. Flach, Quantum caging in interacting many-body all-bands-flat lattices, *Phys. Rev. B* **104**, 085132 (2021).
- [30] I. Vakulchyk, C. Danieli, A. Andreanov, and S. Flach, Heat percolation in many-body flat-band localizing systems, *Phys. Rev. B* **104**, 144207 (2021).
- [31] C. Danieli, A. Andreanov, and S. Flach, Many-body localization transition from flat-band fine tuning, *Phys. Rev. B* **105**, L041113 (2022).
- [32] N. Roy, A. Ramachandran, and A. Sharma, Interplay of disorder and interactions in a flat-band supporting diamond chain, *Phys. Rev. Res.* **2**, 043395 (2020).
- [33] T. Orito, Y. Kuno, and I. Ichinose, Deformation of localized states and state transitions in systems of randomly hopping interacting fermions, *Phys. Rev. B* **105**, 094201 (2022).
- [34] T. Orito, Y. Kuno, and I. Ichinose, Interplay and competition between disorder and flat band in an interacting Creutz ladder, *Phys. Rev. B* **104**, 094202 (2021).
- [35] M. Goda, S. Nishino, and H. Matsuda, Inverse Anderson Transition Caused by Flatbands, *Phys. Rev. Lett.* **96**, 126401 (2006).
- [36] P. Shukla, Disorder perturbed flat bands. II. Search for criticality, *Phys. Rev. B* **98**, 184202 (2018).
- [37] A. Ahmed, A. Ramachandran, I. M. Khaymovich, and A. Sharma, Flat band based multifractality in the all-band-flat diamond chain, *Phys. Rev. B* **106**, 205119 (2022).
- [38] S. Aubry and G. André, Analyticity breaking and Anderson localization in incommensurate lattices, *Ann. Israel Phys. Soc.* **3**, 18 (1980).
- [39] M. Modugno, Exponential localization in one-dimensional quasi-periodic optical lattices, *New J. Phys.* **11**, 033023 (2009).
- [40] C. Danieli, J. D. Bodyfelt, and S. Flach, Flat-band engineering of mobility edges, *Phys. Rev. B* **91**, 235134 (2015).
- [41] V. E. Kravtsov, I. M. Khaymovich, E. Cuevas, and M. Amini, A random matrix model with localization and ergodic transitions, *New J. Phys.* **17**, 122002 (2015).
- [42] E. Bogomolny and M. Sieber, Eigenfunction distribution for the Rosenzweig-Porter model, *Phys. Rev. E* **98**, 032139 (2018).
- [43] D. Facchetti, P. Vivo, and G. Biroli, From non-ergodic eigenvectors to local resolvent statistics and back: A random matrix perspective, *Europhys. Lett.* **115**, 47003 (2016).
- [44] Y. Kuno, T. Orito, and I. Ichinose, Flat-band many-body localization and ergodicity breaking in the Creutz ladder, *New J. Phys.* **22**, 013032 (2020).
- [45] M. Di Liberto, S. Mukherjee, and N. Goldman, Nonlinear dynamics of Aharonov-Bohm cages, *Phys. Rev. A* **100**, 043829 (2019).
- [46] S. Lee, A. Andreanov, and S. Flach, Critical-to-insulator transitions and fractality edges in perturbed flatbands, *Phys. Rev. B* **107**, 014204 (2023).
- [47] N. Macé, F. Alet, and N. Laflorencie, Multifractal Scalings Across the Many-Body Localization Transition, *Phys. Rev. Lett.* **123**, 180601 (2019).
- [48] O. Penrose and L. Onsager, Bose-Einstein condensation and liquid helium, *Phys. Rev.* **104**, 576 (1956).
- [49] T. L. M. Lezama, S. Bera, H. Schomerus, F. Heidrich-Meisner, and J. H. Bardarson, One-particle density matrix occupation spectrum of many-body localized states after a global quench, *Phys. Rev. B* **96**, 060202(R) (2017).
- [50] S. Bera, T. Martynek, H. Schomerus, F. Heidrich-Meisner, and J. H. Bardarson, One-particle density matrix characterization of many-body localization, *Ann. Phys. (Leipzig)* **529**, 1600356 (2017).
- [51] J. Eisert, M. Cramer, and M. B. Plenio, Colloquium: Area laws for the entanglement entropy, *Rev. Mod. Phys.* **82**, 277 (2010).
- [52] N. Laflorencie, Quantum entanglement in condensed matter systems, *Phys. Rep.* **646**, 1 (2016), quantum entanglement in condensed matter systems.
- [53] L. F. Santos and M. Rigol, Onset of quantum chaos in one-dimensional bosonic and fermionic systems and its relation to thermalization, *Phys. Rev. E* **81**, 036206 (2010).
- [54] Y. Y. Atas, E. Bogomolny, O. Giraud, and G. Roux, Distribution of the Ratio of Consecutive Level Spacings in Random Matrix Ensembles, *Phys. Rev. Lett.* **110**, 084101 (2013).
- [55] X. Deng, S. Ray, S. Sinha, G. V. Shlyapnikov, and L. Santos, One-Dimensional Quasicrystals with Power-Law Hopping, *Phys. Rev. Lett.* **123**, 025301 (2019).
- [56] M. Schulz, C. A. Hooley, R. Moessner, and F. Pollmann, Stark Many-Body Localization, *Phys. Rev. Lett.* **122**, 040606 (2019).
- [57] D. J. Luitz, N. Laflorencie, and F. Alet, Many-body localization edge in the random-field Heisenberg chain, *Phys. Rev. B* **91**, 081103(R) (2015).